34th Annual International Conference of the IEEE EMBS
San Diego, California USA, 28 August - 1 September, 2012

Automated Measurement of Pediatric Cranial Bone Thickness and Density from Clinical Computed Tomography*

Kirk Smith, David Politte, *Member, IEEE*, Gregory Reiker, Member, IEEE, Tracy S. Nolan, Charles Hildebolt, Chelsea Mattson, Don Tucker, Fred Prior, *Senior Member, IEEE,* Sergei Turovets and Linda J. Larson-Prior *Member, IEEE*

Abstract— **Skull thickness and density measures of normal pediatric crania would inform multiple disciplines including neurosurgery, optical and magnetoelectrophysiological imaging, and biomechanical modeling of head trauma. We report on a new method for automated extraction of *in vivo* skull thickness and density measures of pediatric crania based on x-ray computed tomography scans (CT). Data were obtained from a clinical image repository for pediatric populations in whom no pathology was noted. Skull thickness and density measures were systematically obtained across the calvarium. We find a set of measures that correlated with physiological age that are likely to prove useful in multiple disciplines.**

I. Introduction

Accurate measures of changes in skull morphometrics across developmental age are of interest to multiple disciplines. From birth to adulthood significant remodeling and growth of tissues make it necessary to define multiple models of skull metrics [1, 2]. Morphometric data from pediatric populations are of value in surgical evaluation of craniofacial deformity [3], in modeling of biomechanical stress due to growth or injury [2, 4], for development of custom bone conduction auditory prostheses [5], and in the creation of head models for source localization in magneto-electroencephalography (M/EEG) and optical imaging [6, 7] However, fontanelles and open sutures in infants produce inhomogeneities in skull conductivity, creating significant distortions in event related potential (ERP) localization [8]. Further, changes in skull height, bone thickness and skull plate composition differ in children from that of adults, making simple scaling of adult head models inappropriate for the production of accurate head models in infants and children [9, 10].

Accurate head models rely in part on measures of skull thickness and density. X-ray computed tomography (CT) is a good source for these measures but is not routinely available in pediatric populations. Furthermore, there is no established method for how and where these measures should be taken. As a result, there is a paucity of information as to how the skull changes during growth, especially in terms of thickness and density. This is the first report of CT derived automated cranial thickness and density measures taken along surface normals from identified soft tissue landmarks. We propose and report results for aligning the head to a particular frame of reference and for a set of automatically defined reference points; but any reference plane identifiable by 3 landmarks, and any point locations desired on the scalp could be used.

II. METHODS

Following an Internal Review Board approved protocol, CT data were mined from the clinical repository at Children's Hospital in St. Louis [11]. The goal was to obtain CT head data of pediatric patients (birth to 18 years of age) where no clinical pathology was indicated. An initial screening of radiology reports, covering the years 2007 to 2011, yielded approximately 300 scans for possible inclusion. These scan data were further reviewed for coverage, resolution, motion artifact, and pathology. For coverage, the scan must contain the top surface of the head and the nasion (NAS), pre-auricular right (PAR), and pre-auricular left (PAL) anatomical landmarks. Resolution was required to be no worse than 1.5 mm slice thickness. Planar slices and 3D renderings of data were assessed for motion artifact and pathology using Analyze software [12]. Exclusion criteria included skeletal deformity, pathology, and prior head surgery. Applying these inclusion/exclusion criteria resulted in a useable data set of 46 subjects.

Those data meeting criteria were de-identified using our in-house developed Clinical Studies Workstation (CSW) software[13] and transferred to a secure data repository.

A. Image Processing

Data reduction was performed using both the Analyze software system and scripts developed in-house using MATLAB (MathWorks, Natick, MA, USA).

*Manuscript received March 15, 2012. This work was supported in part by NIH grant R43 NS67726.

Kirk Smith is with the Washington University School of Medicine, St. Louis, MO 63110 USA (e-mail: smithki@mir.wustl.edu).

David Politte is with the Washington University School of Medicine, St. Louis, MO 63110 USA (e-mail: politted@mir.wustl.edu).

Gregory Reiker is with the Washington University School of Medicine, St. Louis, MO 63110 USA (e-mail: reikerg@mir.wustl.edu).

Tracy Nolan is with the Washington University School of Medicine, St. Louis, MO 63110 USA (e-mail: tracyn@npg.wustl.edu).

Charles Hildebolt is with the Washington University School of Medicine, St. Louis, MO 63110 USA (e-mail: hildeboltc@mir.wustl.edu).

Chelsea Mattson is with the Neuroinformatics Center, University of Oregon, Eugene, OR 97403, USA (e-mail: mattson.chelsea@gmail.com).

Don Tucker is with the Neuroinformatics Center, University of Oregon, Eugene, OR 97403, USA (e-mail: dtucker@egi.com).

Fred Prior is with the Washington University School of Medicine, St. Louis, MO 63110 USA (e-mail: priorf@mir.wustl.edu).

Sergei Turovets is with the Neuroinformatics Center, University of Oregon, Eugene, OR 97403, USA (e-mail: sergei@cs.uoregon.edu).

Linda J. Larson-Prior is with the Washington University School of Medicine, St. Louis, MO 63110 USA (phone: 314-362-7318; fax: 314-362-6971; e-mail: lindap@npg.wustl.edu).

Pre-processing steps were performed using Analyze and included resampling to 0.5 mm cubic voxels using trilinear interpolation, correcting for gantry tilt by applying a shear correction factor, and padding the volume in x, y, or z to accommodate spatial changes during rigid body transformation when aligning to the local reference system.

The measurement pipeline consisted of 3 inputs: a volumetric CT data set, a text file containing three-dimensional coordinates of the 3 landmarks defining the local reference system, and a list of points defining scalp locations from which measurements were made. For our application, we focused on generating information to inform the development of a pediatric head model for ERP source localization. As such, we defined the local reference system using the NAS, PAR, and PAL anatomical landmarks in a manner similar to that of a commercial software package used for ERP localization (Curry, Compumedics Neuroscan). Points on the scalp denoting measurement locations were roughly approximate to the locations of a standard 10-20 array of EEG electrodes (Fig. 1) to achieve a uniform distribution of points over the head.

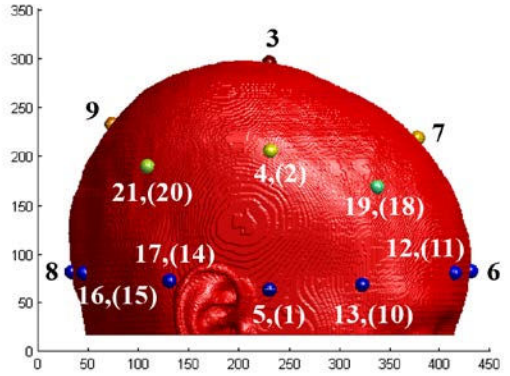

Figure 1: Reference locations where measurements are made. Values in parentheses are on opposite side of the head.

The first stage of the processing pipeline reads the (x,y,z) coordinates of the 3 points defining the local reference system, calculates a rigid body transformation matrix, and transforms the CT image volume using tri-linear interpolation to align the 3 points to a common transverse plane (image slice). This stage ensures a standardized orientation for measurements. The head is isolated from its background using a threshold of -400HU to define the skin, followed by a connect-and-keep operation using a 3x3x3 convolution kernel. This procedure was suitable to segment approximately 75% of cases. The other cases required manual segmentation prior to entering the pipeline. The segmented head is converted to a binary format; a 2D morphological fill is performed in the transverse, sagittal, and coronal planes to fill in the sinuses, and the boundary voxels are extracted.

To automatically locate the measurement points on the head surface, the head is modeled as a hemisphere with its base coplanar to the plane defined by the local reference system and its diameter equal to the distance between the PAR and PAL local reference points. As the head is oblong in shape rather than spherical, the reference hemisphere is translated along the anterior-posterior axis until it is equidistant from the most anterior point of the skull and the most posterior point of the skull as aligned in the local reference system. This also defines a spherical coordinate system that was used to locate the points on the head. The desired locations are input from a file as azimuth and elevation angles in degrees, which are converted to Cartesian coordinates on the surface of the hemisphere. To find the reference point on the surface of the head, a line is projected from the origin as defined by the spherical coordinate system (x1,y1,z1) through a point on the hemisphere specified in Cartesian coordinates (x2,y2,z2). The intersection of that line and the nearest boundary coordinate (x,y,z) located on the surface of the head is taken to be the measurement reference point.

The thicknesses and density measures of the skull are calculated along the surface normals for the set of reference points calculated above (specified by fixed azimuth and elevations relative to the NAS, PAR, PAL reference system and currently numbering 21). For each of these points a convex patch on the surface of the scalp is created (Fig. 2). This stage first cleans up the extracted head surface border by discarding all stray voxels not connected to the actual border. Then, a "seed point," a point on the border (which is closest to the reference point) is identified. Next, a "patch" of points on the border that will be used to fit the sphere is specified. The parameter of the patch size is set by the user and for this application was set to be a radius of 20 mm. The patch is then the set of points on the border that are within 20 mm of the reference point. A patch that is too large may not converge in areas of high curvature whereas a patch with a small radius may be influenced by noise in the data. Finally, the sphere that best fits the voxel patch at a given location is found using the MATLAB function "fminsearch", which performs unconstrained nonlinear optimization based on the simplex search method of Lagarias [14]. This routine optimizes 4 parameters for the sphere, the center xyz-coordinate and its radius by minimizing the sum of squares

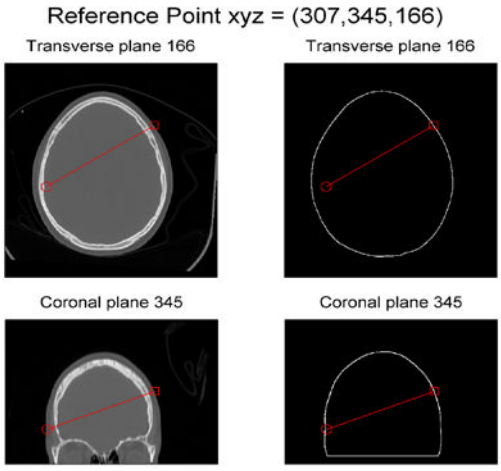

Figure 2: Calculated surface normals projected into transverse and coronal plane on gray scale image (left) and extracted boundary (right). Box is reference location. Circle is center of fitted sphere.

error between the radii of the data points on the patch and of the sphere being fit. These steps are shown in Fig 3.

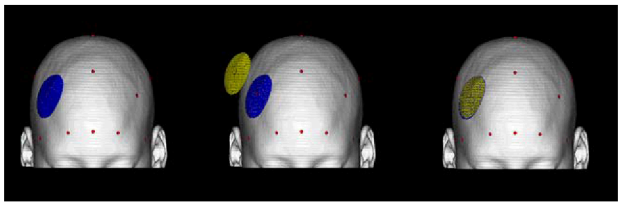

Figure 3: Illustration of spherical patch being fit to selected surface region at a reference point.

The gray-scale data is interpolated along the surface normal and resampled at 0.1 mm voxels using trilinear interpolation. Using the intensity profiles plotted along the surface normals from each reference point, the locations are identified where the 1st derivative (1st difference) crosses zero as shown in Fig 4. The 1st derivative represents local intensity maxima and minima, which are assigned numerical

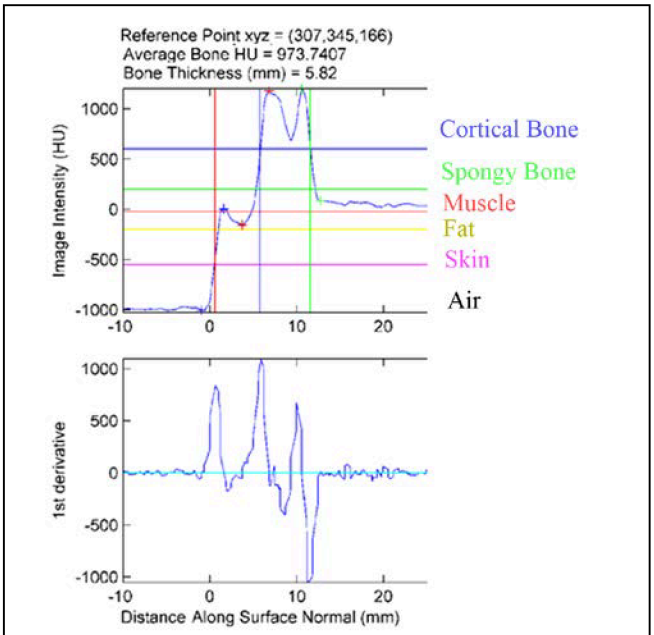

Figure 4: Top- Blue vertical line is outer skull. Green vertical line is cranial vault. Bottom-zero crossings used to determine tissue peaks.

values corresponding to the related tissue according to the intensity value at the crossing. CT image intensities are calibrated in Hounsfield units (HU), which are based on the attenuation coefficient of the tissue; therefore, specific thresholds can be established for tissue types. A bone-soft tissue interface was defined where consecutive zero crossings had different tissue type labels. Partial volume averaging occurs in CT images due to the Gaussian-shaped, point-spread function, and this blurs edge transitions between tissue types. Additionally, if a structure is thinner than the point-spread function used in the reconstruction, the true HU value is not achieved. An accepted method for defining tissue boundaries is to set the threshold value to the mean of the peak values of adjacent tissues. This is the methodology that we used. Bone edges were determined as the half-way point between the maximum and minimum HU values of the adjacent bone and soft tissue peaks. Finally, the skull thickness, defined as the outer-most bony tissue to the innermost bony tissue, is calculated from these edges, and the mean HU value of all voxels that lie between the bone edges are calculated to obtain a measure of bone density. Thick bones with a large diploic component have lower average densities than similar bones with no diploe.

B. *Statistical Methods*

Data distributions were calculated, and tested for normality with the Shapiro-Wilk W Test. Most data distributions (including age) were non-normal (Shapiro-Wilk W Test $P < 0.05$); therefore, to assess the associations between measurement variables and age, scatter plots were created and the Spearman ρ correlation coefficient was calculated. We used a standard scale to rank Spearman ρ correlations: <0.2 is a negligible correlation, 0.2 to 0.4 a low correlation, 0.4 to 0.7 a moderate correlation, 0.7 to 0.9 a high correlation, and >0.9 a very high correlation. We input variables with correlations ≥ moderate into a forward multiple stepwise regression analysis and used the minimal corrected Akaike's information criterion (AICc) [15] to build a model that used measurements of skull thickness and density (in HU) to predict age. To test the model, we performed a maximum K-fold cross validation with a k factor of 3. As an indication of model fit, we plotted residual values against predicted values. Our goal was to select variables that best predicted age. Statistical analyses were performed with JMP Statistical Software Release 9.0.0 (SAS Institute, Inc., Cary, NC).

III. RESULTS

Table 1 indicates the rating scale for correlations of 21 bone thickness (BT) and 21 bone density (HU) measures with physiological age (birth - 18 years). The number following BT or HU represents the measurement location as shown in Fig. 1.

Table 1: Strength of parameter's correlation with age.

Rating	**Correlation with Age**
	Measurement Labels
Very High	BT19, BT3, BT7
High	BT18, BT9, BT21, BT12, BT4, BT2, BT20, BT6, BT11, HU3, HU5, HU19, HU15, HU16, HU7, HU1, HU18
Moderate	BT15, BT16, BT8, HU21, HU20, HU6, HU4, HU10, HU12, HU17, HU14, HU9, HU13, HU2, HU11
Low	BT13, BT14, HU8
Negligible	BT1, BT17, BT5, BT10

Three bone thickness measures had very high correlations with age; 9 bone thickness and 8 density measures had high correlations with age; and 3 bone thickness and 12 bone density measures had moderate correlations with age. Low and negligible correlations with age were found for 5 bone thickness and 1 density measures. Using those measures with moderate to very high correlations with age as input variables to a forward stepwise regression analysis (using minimal AICc and K-fold cross validation), we determined

the model that best predicted physiological age. This analysis demonstrated that BT3, BT4, BT11, BT16 and HU15 were the best predictors of age (Table 2). These correspond to thickness measures of the skull vertex, right parietal bone, left aspect of the frontal bone, right aspect of the occipital bone, and a density measure of the left side of the occipital bone respectively. The adjusted R^2 for the model was 0.92, $p<0.001$. We examined the distribution of residual values on predicted values and they appeared to be randomly scattered about zero.

Table 2: Model parameters kept as best predictors of physiological age.

Term	Parameter Estimates			
	Estimate	Std Error	t Ratio	P
Intercept	-5.1957	0.7581	-6.85	<0.001
BT_3	1.3025	0.1615	8.06	<0.001
BT_4	1.2810	0.3735	3.43	0.001
BT_11	-1.1955	0.384	-3.11	0.003
BT_16	1.0261	0.3011	3.41	0.002
HU_15	0.0029	0.0008	3.66	<0.001

There were three general patterns for the associations between input measurement variables and physiological age (Figs 5). Fig 5 top left is representative of a thickness measurement with negligible correlation with age (Spearman $\rho = 0.02$, $P = 0.88$). This pattern shows little change with increasing age. It is possible that this measurement is not reliable due to large measurement across the population, or it may simply represent a measurement that does not vary with increasing age. Fig 5 bottom right illustrates a thickness measure with moderate correlation with age (Spearman $\rho = 0.62$, $P < 0.001$). This pattern is indicative of a constant rate of change during growth, suggesting that it may be a good growth marker variable in normal pediatric populations. Fig 5 bottom left illustrates a thickness measure with very high correlation with age (Spearman $\rho = 0.91$, $P < 0.001$), exhibiting a rapid change in the measurement variable during the early growth period that lessens with increasing age. This pattern is also characteristic of readily obtained external measures such as skull circumference and cranial index [9].

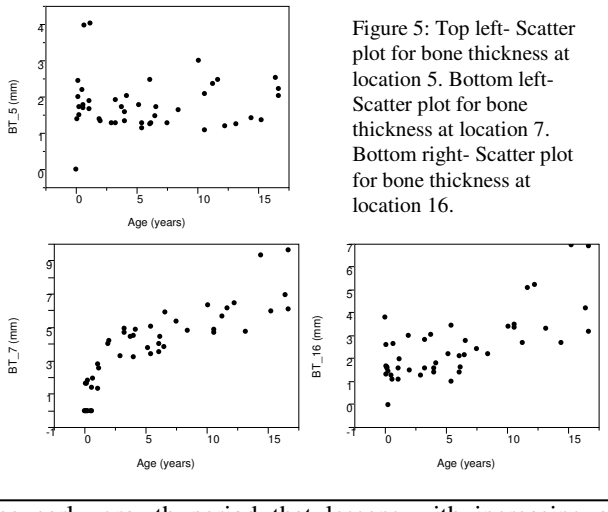

Figure 5: Top left- Scatter plot for bone thickness at location 5. Bottom left- Scatter plot for bone thickness at location 7. Bottom right- Scatter plot for bone thickness at location 16.

IV. CONCLUSIONS

Automated analysis of skull thickness and density (HU) from clinically collected data is feasible. However, data quality in clinical images is generally poor, leading to the requirement for large datasets from which only a small subset may be useful for quantitative analysis. As expected, both bone thickness and density increased with increasing age from birth to 18 years of age. Three general patterns of correlation were found between bone thickness and density and physiological age. Some variables were shown to increase monotonically with age; some had accelerated change during early years of development and slowed with increasing change, while some measures remained relatively constant with age. The methods presented here provide a useful new tool for analysis and modeling of developmental changes in skull morphology and can be applied to a wide range of disciplines in the biomedical sciences to enhance our understanding of cranial development in pediatric populations.

REFERENCES

[1] P. Shaw, N. J. Kabani, J. P. Lerch *et al.*, "Neurodevelopmental Trajectories of the Human Cerebral Cortex," *J. Neurosci.,* vol. 28, no. 14, pp. 3586-3594, April 2, 2008, 2008.

[2] S. S. Margulies, and K. L. Thibault, "Infant Skull and Suture Properties: Measurements and Implications for Mechanisms of Pediatric Brain Injury," *Journal of Biomechanical Engineering,* vol. 122, no. 4, pp. 364-371, 2000.

[3] J. M. Plooij, T. J. J. Maal, P. Haers *et al.*, "Digital three-dimensional image fusion processes for planning and evaluating orthodontics and orthognathic surgery. A systematic review," *International Journal of Oral and Maxillofacial Surgery,* vol. 40, no. 4, pp. 341-352, 2011.

[4] J. H. Henderson, M. T. Longaker, and D. R. Carter, "Sutural bone deposition rate and strain magnitude during cranial development," *Bone,* vol. 34, no. 2, pp. 271-280, 2004.

[5] E. Givelberg, and J. Bunn, "A comprehensive three-dimensional model of the cochlea," *Journal of Computational Physics,* vol. 191, no. 2, pp. 377-391, 2003.

[6] J. Gotman, "Noninvasive Methods for Evaluating the Localization and Propagation of Epileptic Activity," *Epilepsia,* vol. 44, no. s12, pp. 21-29, 2003.

[7] M. D. Holmes, "Dense array EEG: Methodology and new hypothesis on epilepsy syndromes," *Epilepsia,* vol. 49, no. s3, pp. 3-14, 2008.

[8] L. Flemming, Y. Wang, A. Caprihan *et al.*, "Evaluation of the distortion of EEG signals caused by a hole in the skull mimicking the fontanel in the skull of human neonates," *Clinical Neurophysiology,* vol. 116, no. 5, pp. 1141-1152, 2005.

[9] S. Roth, J.-S. Raul, and R. Willinger, "Biofidelic child head FE model to simulate real world trauma," *Computer Methods and Programs in Biomedicine,* vol. 90, no. 3, pp. 262-274, 2008.

[10] S. Roth, J. Vappou, J.-S. Raul *et al.*, "Child head injury criteria investigation through numerical simulation of real world trauma," *Computer Methods and Programs in Biomedicine,* vol. 93, no. 1, pp. 32-45, 2009.

[11] J. Erinjeri, D. Picus, F. Prior *et al.*, "Development of a Google-Based Search Engine for Data Mining Radiology Reports," *Journal of Digital Imaging*, 2008.

[12] R. A. Robb, D. P. Hanson, R. A. Karwoski *et al.*, "Analyze: A Comprehensive, operator-interactive software package for multidimensional medical image display and analysis," *Computerized Medical Imaging and Graphics,* vol. 13, no. 6, pp. 433-454, 1989.

[13] B. Vendt, R. McKinstry, W. Ball *et al.*, "Silent Cerebral Infarct Transfusion (SIT) Trial Imaging Core: Application of Novel Imaging Information Technology for Rapid and Central Review of MRI of the Brain," *Journal of Digital Imaging*, 2008.

[14] J. Lagarias, J. Reeds, M. Wright *et al.*, "Convergence properties of the Nelder-Mead simplex method in low dimensions," *SIAM J Optim* vol. 6, no. 4, pp. 112-147, 1998.

[15] H. Akaike, "Factor analysis and AIC," *Psychometrika,* vol. 52, no. 3, pp. 317-332, 1987.